

# Ultrafast cation-dication dynamics in ammonia borane: H-migration to roaming H<sub>2</sub> and reduced H<sub>3</sub><sup>+</sup> formation under strong-field ionization

Sung Kwon,<sup>†</sup> Naga Krishnakanth Katturi,<sup>†</sup> Bruno I. Moreno,<sup>‡</sup> Carlos Cárdenas,<sup>\*,†</sup> and Marcos Dantus<sup>\*,†,¶,§</sup>

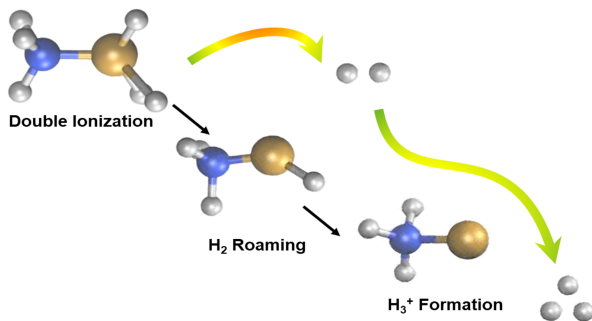
<sup>†</sup>*Department of Chemistry, Michigan State University, 48824 East Lansing, MI, United States*

<sup>‡</sup>*Department of Physics, University of Chile, CEDENNA, Las Palmeras, 3425, Ñuñoa, Chile*

<sup>¶</sup>*Department of Physics and Astronomy, Michigan State University, 48824 East Lansing, MI, United States*

<sup>§</sup>*Department of Electric and Computer Engineering, Michigan State University, 48824 East Lansing, MI, United States*

E-mail: cardena@uchile.cl; dantus@chemistry.msu.edu



## TOC Graphic

## Abstract

We report a femtosecond time-resolved strong-field study of ammonia borane (AB, BH<sub>3</sub>NH<sub>3</sub>) following both single and double ionization, revealing ultrafast fragmentation dynamics and hydrogen release. Mass spectrometry, combined with fragment correlation analysis and *ab initio* molecular dynamics simulations, is used to identify the molecular origin of the neutral and ionic products. Singly ionized AB produces neutral H and H<sub>2</sub>, while doubly ionized AB produces neutral H and H<sub>2</sub> along with H<sup>+</sup>, H<sub>2</sub><sup>+</sup>,

and H<sub>3</sub><sup>+</sup>, all within 1 ps. Electronic-structure calculations show that H, H<sup>+</sup>, H<sub>2</sub>, H<sub>2</sub><sup>+</sup>, and H<sub>3</sub><sup>+</sup> originate predominantly from hydrogen atoms bound to the boron center and that their formation proceeds through hydrogen migration and, in some channels, neutral H<sub>2</sub> roaming. The calculations further indicate that the dication meets the structural and energetic requirements for neutral H<sub>2</sub> release, a prerequisite for forming astrochemically relevant H<sub>3</sub><sup>+</sup>. However, the large adiabatic relaxation energy causes most roaming H<sub>2</sub> to dissociate before proton abstraction, suppressing H<sub>3</sub><sup>+</sup> formation. These results provide new insight into dissociative ionization pathways in hydrogen-rich molecules, extend mechanistic principles developed for halogenated alkanes to ammonia borane, and suggest implications for hydrogen-release chemistry in ammonia-borane-based storage materials.

# TOC Graphic

TOC ENTRY REQUIRED

## Keywords

femtochemistry, molecular dynamics, spectroscopy

## Introduction

Ammonia borane (AB,  $\text{BH}_3\text{NH}_3$ ) has attracted significant attention as a chemical hydrogen storage material due to its exceptionally high hydrogen content, 19.6 wt%, which exceeds that of many conventional storage materials.<sup>1–4</sup> The dehydrogenation process of AB is a key area of research, given its relevance to hydrogen storage applications. Experimental studies have shown that thermal decomposition releases hydrogen in a stepwise manner, forming intermediates such as polyaminoborane and borazine.<sup>5</sup> While most studies have focused on condensed-phase or thermal dehydrogenation behavior of AB, little is known about its gas-phase dynamics under ionizing conditions. The electron-ionization mass spectrum of AB is not available in existing databases, and little is known about its fragmentation behavior upon ionization. In this study, we examine the ultrafast, time-resolved dissociative dynamics of AB following strong-field double ionization.

The chemical bonding in AB involves a dative (coordinate covalent) bond, in which the nitrogen atom donates a lone pair of electrons to the electron-deficient boron atom. The structural properties of AB have been extensively studied to understand its hydrogen storage capabilities. Photoemission and X-ray absorption studies have been conducted to probe its valence and core electronic states, shedding light on the nature of bonding and electronic transitions within the molecule.<sup>6</sup> Theoretical investigations using ab initio molecular dynamics and metadynamics have provided insights into the initial stages of dehydrogenation, suggesting the formation of intermediates like ammonia diborane, which can lead to autocatalytic hydrogen production cycles.<sup>7</sup> Recent studies have also explored the potential of ammonia borane in carbon dioxide capture and conversion.<sup>8,9</sup>

Several molecules have been shown to release  $\text{H}_3^+$  upon double ionization. For example, Eland demonstrated that  $\text{H}_3^+$  can be produced from a range of organic molecules through collisions with high-energy electrons or excitation by 30.4 nm photons.<sup>10</sup> Similarly, Yamanouchi and co-workers (2005–2006) reported  $\text{H}_3^+$  ejec-

tion from gas-phase methanol under intense 800 nm laser fields.<sup>11,12</sup> Complementing these studies, our group has been investigating ultrafast, far-from-equilibrium chemical processes initiated by interactions between molecules and secondary electrons.<sup>13,14</sup> In particular, we have focused on the formation dynamics and mechanisms of  $\text{H}_3^+$  generation from various organic molecules following strong-field ionization.<sup>15–20</sup> Using EUV excitation, Strasser and collaborators have also investigated  $\text{H}_3^+$  formation dynamics in several of these same systems, including methanol and ethanol.<sup>21,22</sup> Despite the prevalence of organic precursors in these studies, only a few non-organic molecules, such as AB examined here, and  $\text{GeH}_4$ , have been shown to generate  $\text{H}_3^+$  upon ionization.<sup>10</sup> The production of  $\text{H}_3^+$  is significant beyond laboratory conditions, it is a key ion in interstellar chemistry, acting as a catalytic proton donor,<sup>23,24</sup> and has recently been proposed as an indirect probe for dark matter.<sup>25</sup> Interestingly, AB is isoelectronic with ethane, a molecule known to readily form  $\text{H}_3^+$  via strong-field dissociation.<sup>26–30</sup> This structural similarity raises questions about the potential of AB to follow analogous dissociation pathways in the gas phase.

## Methods

The ultrafast disruptive-probing method used to monitor all reaction pathways following strong-field ionization has been detailed previously.<sup>31</sup> In this case, a Ti:sapphire laser centered at 795 nm, delivering 65 fs pulses at 1 kHz as measured by in-situ autocorrelation, served as the ionization source. Ammonia borane (95% purity, Sigma-Aldrich) was used without further purification. Laser pulses were focused into a Wiley–McLaren time-of-flight (TOF) mass spectrometer using a 200 mm lens, with polarization aligned parallel to the TOF axis. Each pulse was split into a strong pump pulse to ionize the molecule and a weak probe pulse to disrupt product formation. Laser intensities were calibrated by measuring the  $\text{Ar}^{2+}/\text{Ar}^+$  ion ratio.<sup>32</sup> Ammonia borane vapor was introduced into the TOF chamber as an effusive beam after

a freeze-pump-thaw-cycle. Room-temperature sublimation provided sufficient vapor to obtain the experimental data. During data acquisition, the chamber pressure was held at  $1 \times 10^{-5}$  Torr. The baseline vacuum pressure was  $9 \times 10^{-8}$  Torr and returned to this level within a few seconds of closing the valve. Ion signals were digitized with a 1 GHz oscilloscope (LeCroy WaveRunner 610Zi). The TOF was set to detect cations, so only positively charged ions appear in the mass spectra. To account for the natural isotopic distribution of boron (80%  $^{11}\text{B}$  and 20%  $^{10}\text{B}$ ), peaks containing boron, except the molecular ion, were corrected by 20% to minimize isotope-related contributions. Additionally, contributions from air in the spectrum were removed, using the ratio of ionized  $\text{N}_2^+$  to  $\text{O}_2^+$  in air under identical laser conditions to subtract the  $\text{N}_2^+$  contribution from the m/q 28 signal.

The correlation coefficient analysis with shot-to-shot correction was carried out to account for laser intensity fluctuations. A total of  $N = 39,660$  single-shot mass spectra of AB were acquired and analyzed for this purpose. From the same dataset, the kinetic energy release (KER) distributions for  $\text{H}^+$ ,  $\text{H}_2^+$ , and  $\text{H}_3^+$  were also extracted.

Electronic structure calculations, optimization of the ground state and dication geometries of AB, adiabatic relaxation energies, and  $\text{H}_2$  dissociation energies were carried out at the CCSD(T)<sup>33–36</sup>/aug-cc-pVDZ<sup>37,38</sup> level of theory using GAMESS 2019.R1.<sup>39</sup> The ionization potential calculations for the monocation were done at the CCSD<sup>35,36,40,41</sup>/cc-pVTZ<sup>37,42</sup> and dication were done at the DIP-EOMCC(4h-2p)<sup>43–47</sup>/cc-pVTZ<sup>37,42</sup> level of theory using the same version of GAMESS. All molecular dynamics simulations were performed using Gaussian 09<sup>48</sup> evaluating the force with DFT using the  $\omega$ -B97XD<sup>49</sup> exchange-correlation functional with a 6-311+G(d,p) basis set. To better capture the potential energy of bond breaking processes, a spin broken-symmetry solution was allowed for trajectories. Equations of motion were integrated with Verlet-Velocity and a Hessian-based integrator<sup>50</sup> with step size of 0.5 fs and  $0.25 \sqrt{\text{amu}} * \text{bohr}$ , respectively. For the

cation's AIMD trajectories, atomic positions were taken from a molecular dynamics (MD) simulation of the neutral AB in the NVT (conserving the number of particles, volume, and kinetic energy) ensemble at 300 K (with 0 eV of additional energy). The velocities were sampled from a Maxwell–Boltzmann distribution (thermal sampling), with the constraint that the total kinetic energy of the nuclei was scaled to 1, 1.5, or 7.8 eV. For the case labeled as 0 eV, the velocities were obtained directly from the NVE MD simulation (Maxwell–Boltzmann at 300 K). A total of 100 trajectories were generated for each energy level.

For the dication's AIMD trajectories, two distinct cases were considered. In the first case, a set of 200 trajectories was generated, where the positions and velocities were derived from NVT molecular dynamics simulations of the neutral state (Maxwell–Boltzmann distribution at 300 K). In this scenario, the adiabatic energy is sufficient to promote hydrogen (H) release but not enough to induce Coulomb fragmentation of the boron–nitrogen (B–N) bond. To observe B–N bond fragmentation (second case), 4 eV of energy was selectively injected into the normal mode of  $\text{BH}_3\text{NH}_3^{2+}$  with the largest B–N stretching character, using quasi-classical sampling. This approach was chosen because B–N bond cleavage is a rare event compared to H release, requiring thousands of thermally sampled trajectories to observe it. In some trajectories, fragmentation did not lead to bond breaking but rather to additional hydrogen release, producing  $\text{BHNH}_3^{2+}$ . For these cases, we further injected 4 eV into the B–N stretching mode of  $\text{BHNH}_3^{2+}$ , and so on. Only 25 trajectories were run for these higher-energy cases, as increasing the number of trajectories did not significantly affect the observed trends.

## Results and Discussion

The experimental high-intensity selected strong-field ionization mass spectrum of  $\text{BH}_3\text{NH}_3$  resulting from the difference between two different laser peak intensities of  $3.1 \times 10^{14} \text{ W/cm}^2$  and  $2.7 \times 10^{14} \text{ W/cm}^2$  is shown in

Figure 1a. This difference intensity minimizes contributions from the lower-intensity regions of the Gaussian focal-volume intensity distribution.<sup>51–53</sup> The mass spectrum shows that under strong-field ionization AB can lose all its hydrogen atoms. In addition, dication species are observed at  $m/q$  15.5 ( $\text{M}^{2+}$ ), 14.5 ( $\text{M}-2\text{H}^{2+}$ ), 13.5 ( $\text{M}-4\text{H}^{2+}$ ), and 5.5 ( $\text{B}^{2+}$ ). All smaller

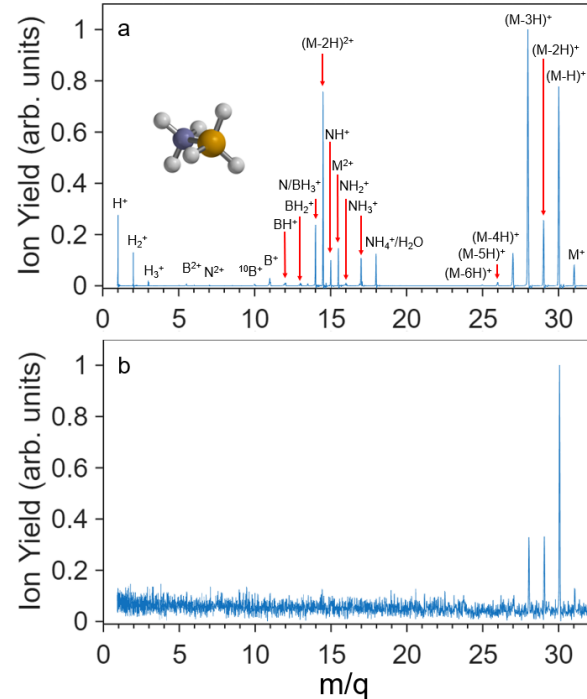


Figure 1: (a) Strong-field ionization mass spectrum of ammonia borane after the difference between two different laser peak intensities of  $3.1 \times 10^{14} \text{ W/cm}^2$  and  $2.7 \times 10^{14} \text{ W/cm}^2$ . Fragment peaks are labeled with their sum formulas. (b) Low-intensity strong-field ionization mass spectrum of ammonia borane taken at an intensity of  $1.3 \times 10^{14} \text{ W/cm}^2$ . Both spectra are normalized to a maximum intensity of 1. M corresponds to the molecular ion.

fragment ions, beginning with  $\text{NH}_3^+$ , exhibit Coulomb-explosion signatures in the time-of-flight spectrum, characterized by distinct forward and backward peaks, except for those at  $m/q$  15.5, 15, 14.5, and 13.5, which appear as single peaks and are assigned as the molecular dication or the molecular dication with the loss of one to three hydrogen atoms. We note that the  $m/q$  15 channel may also contain a contribution from  $\text{NH}^+$ . The low-intensity  $1.3 \times 10^{14} \text{ W/cm}^2$  ionization mass spectrum is shown in Figure 1b. This spectrum shows that even at low intensities, AB loses one or more H atoms. The high yield of  $m/q$  30, corresponding to loss of a single hydrogen atom, is attributed to the

small energy gap between the adiabatic ionization potential of AB (9.6 eV) and the threshold for the first H-atom loss (10.0 eV).<sup>54</sup> Hydrogen loss is quantified in Tables 1 and 2 from the integrated peak areas for the monocation and dication, respectively, and both tables show that hydrogen loss is frequent following both single and double ionization.

**Table 1:** The experimental integrated areas of  $m/q$  fragments corresponding to H loss normalized by the sum of the total integrated area of all peaks at an intensity of  $1.3 \times 10^{14} \text{ W/cm}^2$ .

$m/q$	Area (% of Monocations)
31	7.5
30	38.6
29	13.9
28	32.8
27	7.3

**Table 2:** The experimental areas of  $m/q$  fragments corresponding to loss of  $2\text{H(s)}$  normalized to the total area of dication peaks at an intensity of  $3.1 \times 10^{14} \text{ W/cm}^2$ .

$m/q$	Area (% of Dications)
15.5	15.3
14.5	80.2
13.5	1.4

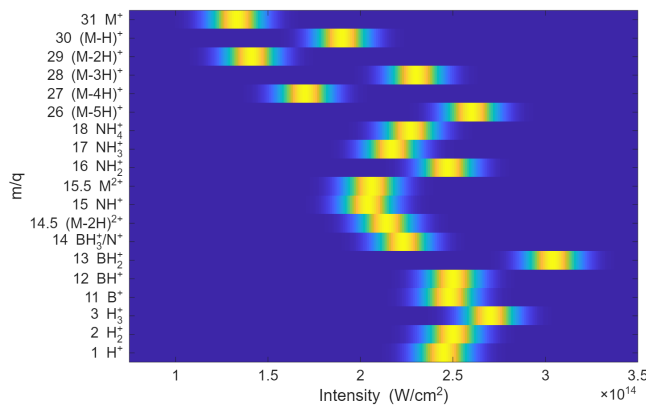


**Figure 2:** Heat map of the major AB fragment yields as a function of calibrated laser intensity. The appearance-intensity thresholds, which are proportional to the corresponding appearance energies, were extracted using the procedure described in the Supporting Information (Figure S1). The width of each onset feature reflects the uncertainty in the threshold determination and thus provides a measure of confidence.

Dissociative ionization was further examined through calibrated<sup>32</sup> laser power dependence in

Figure 2, where each successive data point corresponds to a higher intensity. For each fragment, we compute the numerical difference in integrated yield between adjacent points (i.e. point  $n+1$  minus point  $n$ ), which suppresses the focal-volume contribution. The resulting difference trace is then fit with an error function. The appearance of each fragment was determined by the laser peak intensity at which its yield exceeded 10% of the maximum (see Figure S1).

When photoionization occurs within a single optical cycle or faster, the liberated electron gains kinetic energy proportional to the peak intensity. The ponderomotive energy, which scales linearly with intensity, governs the electron's motion, driving it away from the ion and back toward it as the laser field reverses.<sup>55</sup> In general, the intensity required for ion formation can be directly related to the fragment's appearance energy (AE). Upon recollision, the electron transfers energy to the molecule, inducing ionization, fragmentation, and in some cases, double ionization. The calculated single and double vertical ionization potentials for AB were calculated to be 11.9 eV and 31.1 eV, *vide infra* at the CCSD<sup>40,41</sup>/cc-pVTZ<sup>37,42</sup> and DIP-EOMCC(4h-2p)<sup>43-47</sup>/cc-pVTZ<sup>37,42</sup> respectively. In general, we see that losing pairs of hydrogen atoms requires less energy compared to single or triple hydrogen loss. Unlike most hydrocarbons,<sup>56</sup>  $\text{H}^+$  loss from AB is observed only when the laser intensity is high enough to cause double ionization. Note that fragments resulting from breaking the B-N bond ( $m/q$  18, 17, 16, 14, 13, 12, and 11) exceed the appearance energy of the dication.

The ultrafast formation dynamics of all ionic species were simultaneously measured using disruptive probing, a technique where an intense pump pulse ionizes the molecule and a time-delayed weak probe pulse disrupts its fragmentation.<sup>31</sup> The probe pulse by itself causes no ionization. The resulting ion yields as a function of pump-probe delay time enable the simultaneous tracking of all fragmentation pathways and products.<sup>31</sup> Figure 3 shows the ion yield as a function of pump-probe delay for all major fragments of AB.

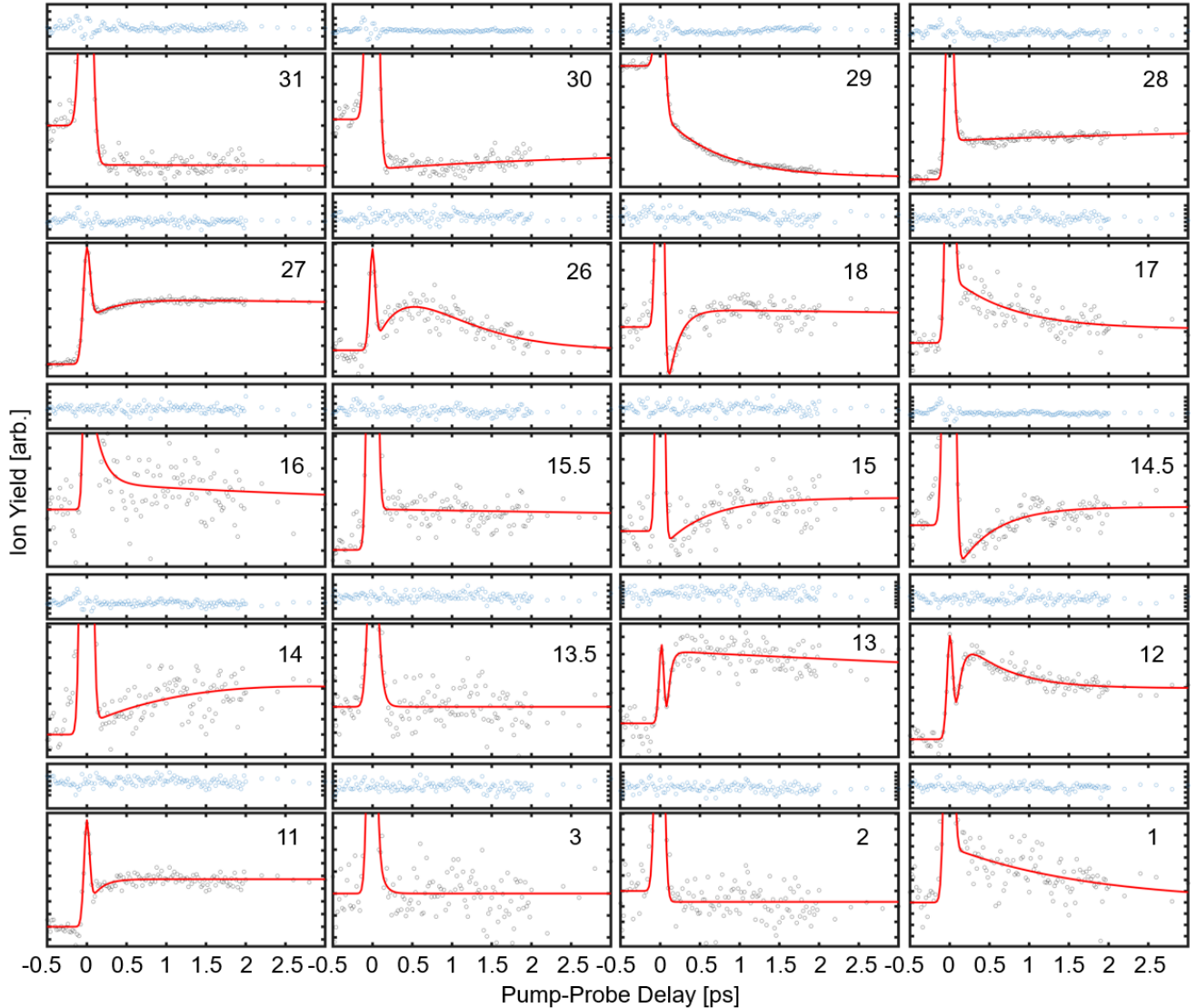


Figure 3: Ion yield as a function of pump-probe delay for all major  $m/q$  with the residual plotted above. The time-resolved data was acquired at a pump intensity of  $3.1 \times 10^{14} \text{ W/cm}^2$  and probe intensity of  $4.4 \times 10^{13} \text{ W/cm}^2$ .

The time-dependent yield of the selected fragments exhibit a narrow feature at zero time delay, corresponding to the spatial and temporal overlap of the pump and probe pulses, as shown in Figure 3. At asymptotic pump-probe delays, the ion yields for  $m/q$  31, 30, and 29 remain reduced relative to their negative-delay baselines. In contrast, the yields of all other major fragments either (i) recover to the negative-delay value—indicating that, at long delays, the probe no longer measurably perturbs their formation or depletion—or (ii) increase above the baseline, consistent with probe-induced formation from a long-lived precursor. At early (sub-picosecond) delays, transient depletions or enhancements reflect probe perturbation of the

evolving reaction dynamics; fitting these transients provides an effective formation timescale for the corresponding product. Owing to the low signal-to-noise ratio, we could not reliably extract a formation timescale for  $\text{H}_3^+$ . Loss of two hydrogens leading to  $m/q$  29 displays a depletion with a time constant of  $340 \pm 65 \text{ fs}$  and a long offset term, while loss of four hydrogens leading to  $m/q$  27 shows a fast rise with a  $340 \pm 100 \text{ fs}$  time constant and a long offset term. The similarity between these timescales suggests that both two- and four-hydrogen loss channels proceed through closely related dynamics. On the other hand, the loss of five hydrogen atoms leading to  $m/q$  26 shows a rapid enhancement with a  $175 \pm 10 \text{ fs}$  time constant,

**Table 3: Exponential fit parameters for all  $m/q$  ion dynamics from AB.**

$m/q$	$\tau_1$ (fs)	$\tau_2$ (fs)	$\tau_3$ (fs)	$a_1$	$a_2$	$a_3$
31	$92 \pm 10$	offset	-	0.01	-0.004	-
30	$250 \pm 180$	$10000 \pm 530$	-	-0.002	0.0008	-
29	$340 \pm 65$	offset	-	0.01	-0.01	-
28	$3500 \pm 1300$	offset	-	-0.004	0.01	-
27	$340 \pm 100$	offset	-	-0.001	0.004	-
26	$175 \pm 10$	$810 \pm 35$	-	0.02	-0.03	-
18	$140 \pm 47$	offset	-	-0.02	0.002	-
17	$720 \pm 75$	offset	-	0.005	0.003	-
16	$130 \pm 20$	$5100 \pm 2300$	-	0.01	.003	-
15.5	offset	-	-	0.004	-	-
15	$640 \pm 78$	offset	-	-0.005	0.003	-
14.5	$480 \pm 55$	offset	-	-0.006	0.002	-
14	offset	-	-	0.002	-	-
13.5	$40 \pm 32$	-	-	0.4	-	-
13	$40 \pm 40$	offset	-	-0.1	0.02	-
12	$80 \pm 44$	$480 \pm 270$	offset	-0.07	0.02	-0.02
11	$120 \pm 16$	offset	-	0.02	-0.01	-
3	offset	-	-	0.004	-	-
2	$230 \pm 170$	-	-	0.002	-	-
1	$400 \pm 200$	-	-	0.005	-	-

followed by a slower decay with a  $810 \pm 35$  fs time constant. A similar enhancement is observed for  $m/q$  13 and 12, though it occurs more rapidly, with time constants of  $40 \pm 40$  fs and  $80 \pm 44$  fs, respectively. The formation of  $\text{NH}_4^+$  ( $m/q$  18) is characterized by a time constant of  $140 \pm 47$  fs. This rapid hydrogen migrations from boron to nitrogen occurs on a timescale consistent with previously reported H-transfer dynamics.<sup>57–59</sup> All the fitting constants are provided in table 3. In certain cases ( $m/q = 29, 27$ , and  $26$ ), the dynamics were corrected for contamination from  $^{10}\text{B}$ . This correction, applied from high to low  $m/q$ , was based on isotope contributions estimated from the  $^{11}\text{B}$ -corrected fragment signal. Specifically, the ion yield of the affected  $m/q$  was scaled at each time delay using its corresponding correction factor. For  $m/q$  31, 30, 28, and 26, isotope contributions were less than 3% and thus not corrected. The dynamics observed under high-intensity conditions closely match those at low intensity (see Figure S2), indicating that fragments in the  $m/q$  26–31 range predominantly arise from monocationic AB, even at high inten-

sity. The dication corresponding to  $(\text{M}-2\text{H})^{2+}$  exhibits a depletion with a time constant of  $230 \pm 43$  fs, consistent with  $\text{H}_2$  loss. Dicationic fragments at  $m/q$  15.5 and 13.5 show no discernible time-resolved dynamics.

Fragment correlation mass spectrometry is a technique to infer common parentage, concerted breakup, or reaction pathways among ions.<sup>60–62</sup> We measured the dissociative ionization of AB fragment ions at an intensity of  $3.1 \times 10^{14} \text{ W/cm}^2$ , while keeping the background pressure at  $10^{-7}$  Torr. We acquired 39,660 single shot mass spectra and analyzed the correlation coefficients of all the fragments. For  $m/q$  2, 11, 12, 13, 14, 16, and 17, the signals exhibit clear forward–backward splitting (see Figure S3). To isolate contributions from dicationic channels, only the wings of these peaks were used in the correlation analysis. To account for shot-to-shot fluctuations, the ion signals from all fragments were summed and used for normalization. The resulting correlation coefficient matrix is shown in Figure 4. In the absence of shot-to-shot fluctuation correction, nearly all fragments exhibit spurious positive

correlations, as illustrated by the uncorrected matrix in the Supporting Information (see Figure S4).

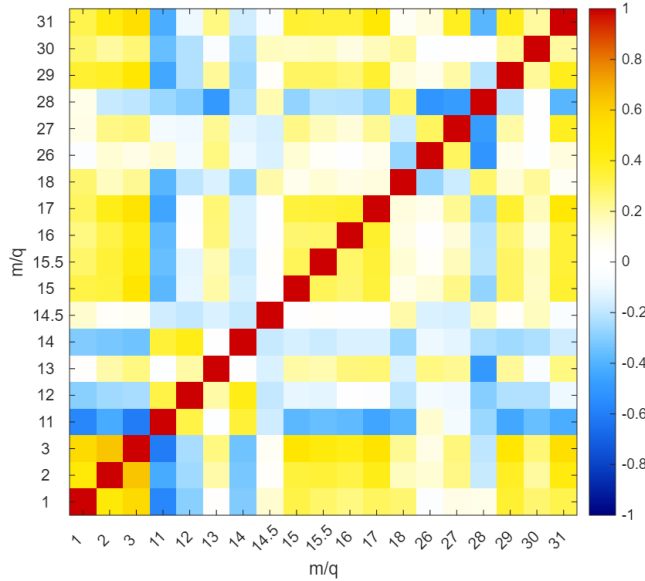


Figure 4: The calculated correlation coefficients from  $N = 39,660$  single-shot mass spectra of AB after shot-to-shot corrections.

Analysis of single-shot mass spectra of AB following dissociative double ionization provides insight into the origin of  $\text{H}_2$  loss and subsequent fragment formation. We observe positive correlation signals between  $\text{H}^+$ ,  $\text{H}_2^+$ , and  $\text{H}_3^+$  and  $\text{NH}_n^+$  ( $n = 1-3$ ). These correlations indicate that the hydrogens forming  $\text{H}^+$ ,  $\text{H}_2^+$ , and  $\text{H}_3^+$  through  $\text{H}_2$  loss predominantly originate from the boron end of the molecule.

The time-of-flight arrival of  $\text{H}^+$ ,  $\text{H}_2^+$ , and  $\text{H}_3^+$ , can be further analyzed to determine their kinetic energy release (KER). In our experiments, the laser polarization was oriented parallel to the time-of-flight (TOF) axis. Because ammonia borane has a strong permanent dipole moment, molecules with their dipole aligned along the laser polarization are expected to ionize most efficiently. As a result, we anticipate strongly polarized forward–backward ejection of the  $\text{H}_n^+$  fragments along the polarization (TOF) axis.

The fragment-ion kinetic energy,  $E_{\text{ion}}$ , was obtained from the time separation between the forward and backward peaks,  $\Delta t$ , according to

$$E_{\text{ion}} = \frac{q^2 F^2 (\Delta t)^2}{8m}, \quad (1)$$

where  $q$  is the fragment charge,  $F$  is the static extraction field,  $\Delta t$  is the forward–backward flight-time difference, and  $m$  is the fragment mass. To convert this value to the total kinetic energy release (KER) of the two-body breakup, we account for recoil of the complementary fragment with mass  $M - m$ , where  $M$  is the parent-ion mass, using

$$E_{\text{total}} = E_{\text{ion}} \left( 1 + \frac{m}{M - m} \right). \quad (2)$$

These expressions were used consistently for all reported KER values. As shown in Figure 5, the KER distributions for  $\text{H}^+$ ,  $\text{H}_2^+$ , and  $\text{H}_3^+$  exhibit prominent peaks at 5.7, 6.1, and 5.8 eV, respectively. These values are consistent with Coulomb explosion following double ionization and are comparable to the KER expected for doubly ionized methanol (5.0 eV if all three H atoms originate from carbon and 5.48 eV if one H atom originates from oxygen).<sup>15</sup> Because KER is highly sensitive to the interatomic distance at the moment of charge separation, even small changes in geometry can shift the peak substantially; for example, the KER for  $\text{N}_2$  is 6.5 eV.<sup>63</sup> In addition to the low-KER peaks,  $\text{H}_2^+$  and  $\text{H}^+$  show higher-energy peaks at 13 and 18 eV, respectively, consistent with fragmentation from more highly charged precursors. Similar high-KER channels have been reported for trications, including triply ionized ethylene at  $8 \times 10^{14} \text{ W/cm}^2$ , which produces a peak near 11 eV,<sup>64</sup> and triply ionized acetylene, for which the total KER is 15 eV.<sup>65</sup>

Using the Coulomb repulsion expression inverted to estimate the charge-separation distance at explosion, we extract mean fragment separations of 2.5, 2.1, and 2.24 Å for the doubly ionized channels producing  $\text{H}^+$ ,  $\text{H}_2^+$ , and  $\text{H}_3^+$ , respectively, and 1.7 and 2.0 Å for the higher-energy channels assigned to trication precursors producing  $\text{H}$  and  $\text{H}_2$ , respectively. Because the pulses used here are relatively long, bond stretching can occur during the ionization sequence, which favors enhanced ionization at extended bond lengths.<sup>66</sup> The observation of  $\text{H}^+$  kinetic energy release extending beyond 40 eV is consistent with fragmenta-

tion from a highly charged precursor accessed through sequential ionization via enhanced ionization, potentially promoted by proton migration and the associated transient charge localization. If enhanced ionization in this system is promoted by bond stretching, then employing sub-10 fs pulses that are too short for appreciable stretching should curtail the enhanced-ionization pathway and decrease the yield of very high charge states. We plan to test this expectation directly using our recently commissioned 5 fs laser pulses.

Finally, only  $\text{H}_2^+$  exhibits a near-zero-KER peak. Although a zero-KER component could suggest formation from the monocation, the laser-intensity dependence in Figure 2 indicates that  $\text{H}_2^+$  appears predominantly at higher intensities and therefore correlates with dication formation. We therefore attribute the zero-KER  $\text{H}_2^+$  signal to ionization of neutral  $\text{H}_2$  (ionization energy 15.4 eV) after it dissociates from the monocation within the same 65 fs laser pulse, before the departing fragments acquire significant relative kinetic energy.

Previous work has shown that the production of  $\text{H}_3^+$  from methyl pseudohalogens and halogens ( $\text{CH}_3\text{X}$ ) via the  $\text{H}_2$  roaming mechanism<sup>15,16</sup> is governed by three key factors.<sup>20</sup> These are summarized below:

1. Double ionization leads to a significant elongation of two C–H bonds compared to the neutral  $\text{CH}_3\text{X}$  molecule.
2. In the lowest singlet state of  $\text{CH}_3\text{X}^{2+}$ , the distance between the two hydrogen atoms with the elongated bonds should approximate the ground state  $\text{H}_2$  bond length.
3. The adiabatic relaxation energy, defined as the energy difference between the Franck–Condon point (vertical ionization) and the lowest singlet state of the dication, must exceed the dissociation energy of neutral  $\text{H}_2$  for its release, a key step in the roaming pathway, but it cannot be so large that other reactive pathways or decomposition mechanisms compete significantly.

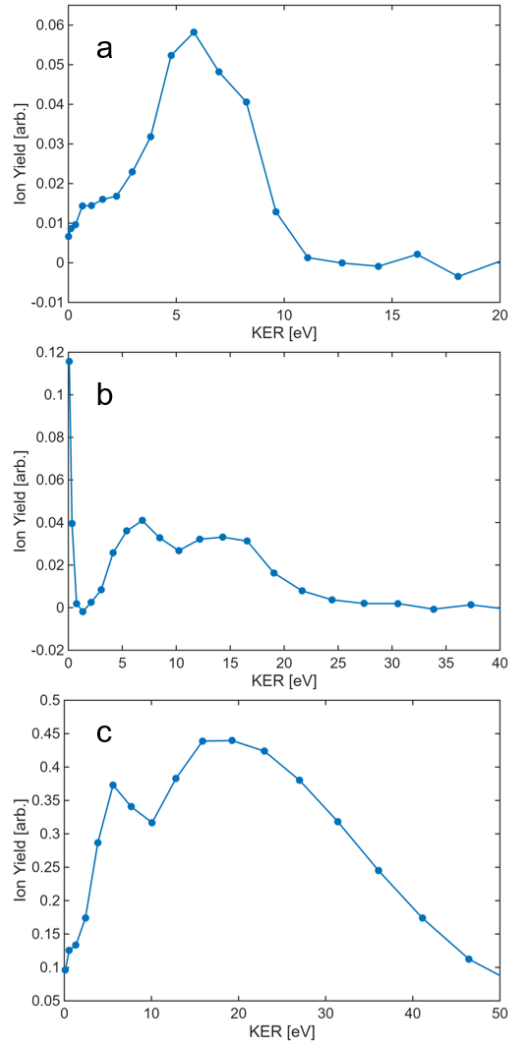


Figure 5: The experimental KER spectra of (a)  $\text{H}_3^+$ , (b)  $\text{H}_2^+$ , and (c)  $\text{H}^+$ . Blue dots represent the measured data, while the blue line serves as a guide to the eye.

Although AB is not a  $\text{CH}_3\text{X}$  compound, these governing principles may extend to other molecules, such as ethane,<sup>20</sup> which upon double ionization undergoes H-atom migration and the  $\text{CH}_2\text{CH}_4^{2+}$  species releases  $\text{H}_2$  which roams and abstracts a proton to form  $\text{H}_3^+$ .<sup>30</sup> To determine if AB, which is isoelectronic with ethane, fulfills these requirements, electronic structure calculations were carried out using GAMESS 2019.R1<sup>39</sup> at the CCSD(T)<sup>35</sup>/aug-cc-pVQZ<sup>37,38</sup> level of theory. Comparing the ground state and dication geometries of AB, shown in Figure 6, one notices the significantly elongated B–H bonds relative to neutral AB, thus satisfying the first criterion.

Additionally, the hydrogens involved in the elongated bonds of the lowest singlet state of

$\text{AB}^{2+}$  have an internuclear distance of 0.80 Å comparable to the 0.74 Å bond length of molecular  $\text{H}_2$ , thus fulfilling the second condition. The adiabatic relaxation energy of  $\text{AB}^{2+}$  (7.17 eV) is much higher than the  $\text{H}_2$  dissociation energy (1.23 eV), similar to  $\text{CH}_3\text{F}^{2+}$  (4.5 and 2.2 eV, respectively).<sup>20</sup> The larger energy difference in  $\text{AB}^{2+}$  favors neutral  $\text{H}_2$  release and results in a low  $\text{H}_3^+$  yield, similar to  $\text{CH}_3\text{F}^{2+}$ .<sup>67</sup> Nevertheless, the observation of  $\text{H}_3^+$  from AB indicates that the same governing factors extend beyond methyl pseudohalogens and halogens, enabling a framework for predicting when  $\text{H}_2$  release will lead to appreciable  $\text{H}_3^+$  formation and providing additional insight into the mechanisms of  $\text{H}_2$  release and subsequent  $\text{H}_3^+$  production in AB.

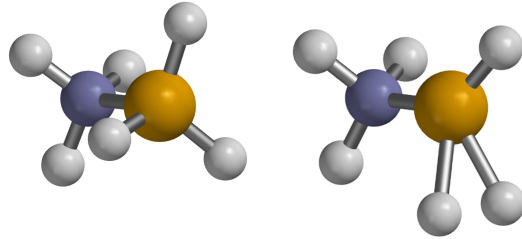


Figure 6: The ground state geometry of the AB neutral (left) and dication (right), visualized using Spartan '24.<sup>68</sup> The nitrogen atom is blue and the boron atom is tan.

We performed ab initio molecular dynamics (MD) simulations for both the singly and doubly charged cations of  $\text{BH}_3\text{NH}_3$ , using 300 independent trajectories conserving the number of particles, volume, and energy. In all cases, the initial atomic positions and velocities were sampled from a 300 K MD simulation of the neutral parent molecule, so the maximum energy available for fragmentation corresponds to the adiabatic relaxation energy following ionization.

Under these conditions, the singly charged cation rarely undergoes hydrogen loss, likely due to the 0.74 eV H-bond dissociation energy.<sup>54</sup> AIMD trajectories of the monocation were performed with total nuclear kinetic energies of 0, 1, 1.5, and 7.8 eV. 7.8 eV was chosen because the energy difference between the  $1e_1$  state and the ground state of the AB cation is 7.76 eV. The 1 and 1.5 eV trajectories were extended to 2 ps in order to capture fragmenta-

tion pathways occurring on longer timescales. The results of monocation AIMD trajectories are summarized in Figure 7. As the total kinetic energy increases, the yield of intact AB decreases while H and/or  $\text{H}_2$  loss becomes more prominent. This dissociation originates exclusively from the boron end of the molecule up to 7.8 eV of deposited energy, consistent with the lower bond dissociation energy of B–H relative to N–H bonds. The increased yield of  $m/q$  30, corresponding to the loss of one H, with increasing internal energy is consistent with the high experimental yield observed for  $m/q$  30.

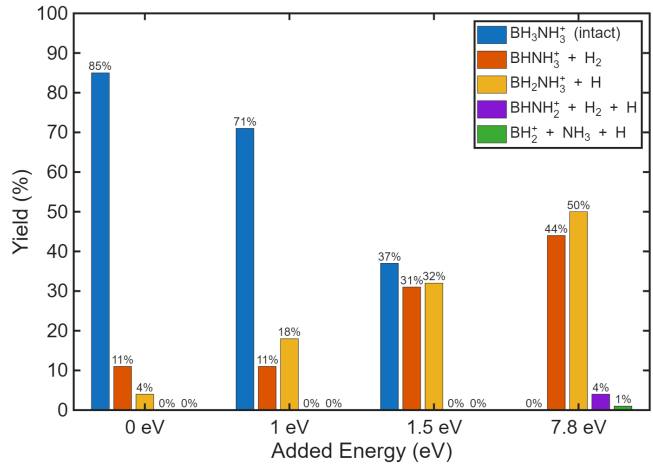
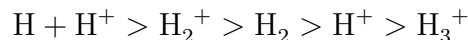


Figure 7: The AIMD trajectory results for the monocation for 0, 1, 1.5, and 7.8 eV kinetic energy.

Furthermore, we performed AIMD trajectories for the dication (see Movie 1 for a  $\text{H}_3^+$  formation trajectory, Movie 2 for a B–N bond cleavage trajectory, Movie 3 for a  $\text{H}_3^+$  formation trajectory following H scrambling, and Figure S5 for snapshots of these trajectories). After 1 ps, 95% of the  $\text{BH}_3\text{NH}_3^{2+}$  trajectories exhibit hydrogen loss, with product yields following the trend:



(see Table 4). Following hydrogen loss,  $\text{BHNH}_3^{2+}$  is the most relevant dication for subsequent fragmentation.

The average kinetic energy of nascent  $\text{BHNH}_3^{2+}$  is 1.7 eV, which is insufficient to cleave the B–N bond (dissociation energy  $\sim$ 3.7 eV, see Figure S6). However, this barrier can be overcome experimentally through laser-induced electron recollision. At the laser

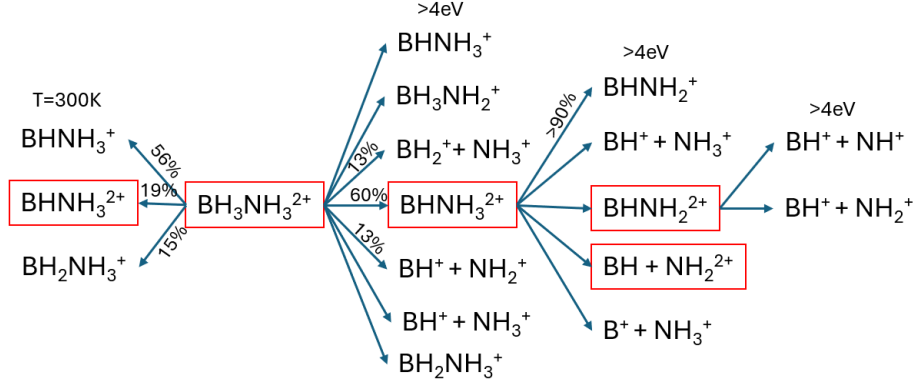


Figure 8: Fragmentation pathways of the doubly charged cation  $\text{BH}_3\text{NH}_3^{2+}$  (red rectangles) following sequential dissociation events. Values accompanying arrows indicate the fraction of trajectories resulting in each specific fragment or set of fragments. Released H's are not indicated for clarity. Numbers on top of each column denote the minimum vibrational energy (in eV) injected into the parent cation during the initial momentum assignment. The leftmost column corresponds to a purely thermal sampling at 300 K, with no additional vibrational energy. Only the most abundant products and primary pathways are shown.

intensities used here, the recollision energy can exceed 50 eV, which rapidly redistributes as electronic and vibrational excitation. To simulate such conditions and explore B-N bond dissociation, we performed additional MD trajectories for vibrationally excited dications. In these simulations, vibrational energy was injected by either: (i) distributing 5 or 7 eV of kinetic energy among all atoms according to a Boltzmann distribution, or (ii) selectively allocating 4 eV into the normal mode with the largest B-N stretch character (using quasi-classical sampling<sup>69</sup>).

The resulting fragmentation pathways are summarized in Figure 8, which shows that H loss in the form of  $\text{H}^+$ , H,  $\text{H}_2^+$ , and  $\text{H}_2$  are predominantly released from the boron atom. This is in agreement with the positive correlation signal observed between  $\text{H}^+$ ,  $\text{H}_2^+$ , and  $\text{H}_3^+$  and  $\text{NH}_n^+$  ( $n = 1-3$ ). Even when 4 eV are in-

jected into the vibrational mode that stretches the B-N bond,  $\text{H}_2$  is formed approximately 60% of the time. The molecular dynamics simulations support the following assignments for the strong-field ionization mass spectrum: *i*) most abundant dication,  $(M - 2H)^{2+}$ , corresponds to  $\text{BHNH}_3^{2+}$ . *ii*) Most abundant cation,  $(M - 3H)^+$ , corresponds to  $\text{BHNH}_2^+$ . *iii*)  $\text{NH}_3^+$  and  $\text{NH}_2^+$  can be formed from Coulomb explosion through two channels, while  $\text{NH}^+$  is only significantly observed from fragmentation of  $\text{BNH}_2^{2+}$ . This explains why  $\text{NH}_3^+$  is as abundant as  $\text{NH}_2^+$  and more than  $\text{NH}^+$ .

In general, we never observe a trajectory resulting in  $\text{BH}_3^+$ , which suggests that the peak in the mass spectrum at  $m/q = 14$  primarily corresponds to  $\text{N}^+$ . Works on the catalytic dehydrogenation of neutral AB show that it is easier to abstract H from B than N,<sup>70</sup> consistent with our findings. Summarizing, MD suggests

Table 4: Primary hydrogen-release channels from  $\text{BH}_3\text{NH}_3^{2+}$  observed from ab initio molecular dynamics (MD) simulations. Initial atomic positions and velocities were sampled from a 300 K MD trajectory of neutral  $\text{BH}_3\text{NH}_3$ . After ionization, trajectories of the dication were propagated in the NVE ensemble.

Channel	Yield	Time [fs]
$\text{BH}_3\text{NH}_3^{2+} \rightarrow \text{intact}$	5%	-
$\text{BH}_3\text{NH}_3^{2+} \rightarrow \text{BHNH}_3^+ + \text{H} + \text{H}^+$	33%	$73 \pm 55$
$\text{BH}_3\text{NH}_3^{2+} \rightarrow \text{BHNH}_3^+ + \text{H}_2^+$	23%	$134 \pm 74$
$\text{BH}_3\text{NH}_3^{2+} \rightarrow \text{BHNH}_3^{2+} + \text{H}_2$	19%	$194 \pm 120$
$\text{BH}_3\text{NH}_3^{2+} \rightarrow \text{BH}_2\text{NH}_3^+ + \text{H}^+$	15%	$47 \pm 23$
$\text{BH}_3\text{NH}_3^{2+} \rightarrow \text{BNH}_3^+ + \text{H}_3^+$	0.5%	-
$\text{BH}_3\text{NH}_3^{2+} \rightarrow \text{BHNH}_2^+ + \text{H}_3^+$	3.5%	$299 \pm 127$

that upon double ionization,  $\text{BH}_3\text{NH}_3^{2+}$  undergoes H-atom/ $\text{H}_2$ -molecule elimination prior to Coulomb explosion yielding  $\text{BH}^+ > \text{BH}_3^+$ , and  $\text{NH}_3^+ \sim \text{NH}_2^+ > \text{NH}^+$  fragments. Also, under single ionization, atomic and molecular hydrogen are most likely released as neutral species.

## Conclusions

In conclusion, we performed time-resolved strong-field ionization of ammonia borane and analyzed its ultrafast fragmentation dynamics. Hydrogen release was observed from both monocationic and dicationic species and occurs on sub-picosecond timescales. Through disruptive probing, we identified that the loss of two and four hydrogen atoms, corresponding to  $m/q$  29 and 27, originates from a common fragmentation pathway and proceeds sequentially. The released hydrogen species predominantly originate from the boron site. Notably, the monocation produces only neutral H and  $\text{H}_2$ . Fragment correlation analysis identifies the boron center as the primary source of  $\text{H}^+$ ,  $\text{H}_2^+$ , and  $\text{H}_3^+$ . The data obtained also enables the determination of their respective kinetic energy release distributions.

High-level electronic structure calculations were used to determine the first and second ionization potentials of AB, as well as the adiabatic relaxation energy and geometry of the lowest singlet state of the dication. These confirm the AB dication satisfies the structural and energetic criteria for  $\text{H}_2$  release, a prerequisite for forming  $\text{H}_3^+$ . However, the high adiabatic energy causes most  $\text{H}_2$  molecules to leave instead of roaming and abstracting a proton. These results extend principles established for the formation of  $\text{H}_3^+$  via the  $\text{H}_2$  roaming mechanism for methyl halogens and pseudo-halogens to AB, improving our understanding of far-from-equilibrium chemical processes under strong-field conditions.

AIMD trajectories of the dication reveal extensive H scrambling and  $\text{H}_3^+$  formation via a neutral roaming  $\text{H}_2$  intermediate, while also showing that B–N bond cleavage requires substantially higher energy; consistent with exper-

iment, as the earliest H loss is initiated from the borane end of the molecule. Given the high hydrogen content of AB and its importance as a promising chemical hydrogen storage material, understanding its gas-phase ionization and fragmentation dynamics provides valuable insight into its dissociative behavior and potential applications.

## Supporting Information

The Supporting Information is available free of charge at: [DOI] It contains: (1) Details about how the threshold laser intensity proportional to the appearance energies were estimated (S-1); (2) Comparison of high and low Intensity dynamics for  $m/q$  29 (S-3); (3) Average of 39,660 mass spectra of AB used for calculating the correlation matrix (S-4); (4) Resulting correlation matrix analysis without shot-to-shot corrections (S-5); (5) AIMD Movie snapshots for three trajectories (S-7); (6) Cuts along the potential energy surface as a function of B–N bond distance (S-8); and (7) Table with primary hydrogen-release channels from AB (S-9).

## Acknowledgements

This material is based on work supported by the Air Force Office of Scientific Research under award number FA9550-21-1-0428 for the study of ultrafast dynamics induced by secondary electrons. S.K. acknowledges partial funding from the U.S. Department of Energy, Office of Science, Office of Basic Energy Sciences, Atomic, Molecular, and Optical Sciences Program, under SISGER DE-SC0002325. C.C. acknowledges ANID for the grants FONDECYT 1220369 and CEDENNA CIA250002. S.K. acknowledges S. Priyadarshini for her help in setting up the GAMESS calculations. Powered@NLHPC: This research was partially supported by the supercomputing infrastructure of the NLHPC (CCSS210001).

## References

(1) Chen, P.; Zhu, M. Recent progress in hydrogen storage. *Materials today* **2008**, *11*, 36–43.

(2) Graetz, J. New approaches to hydrogen storage. *Chemical Society Reviews* **2009**, *38*, 73–82.

(3) Sutton, A. D.; Burrell, A. K.; Dixon, D. A.; Garner III, E. B.; Gordon, J. C.; Nakagawa, T.; Ott, K. C.; Robinson, J. P.; Vasiliu, M. Regeneration of ammonia borane spent fuel by direct reaction with hydrazine and liquid ammonia. *Science* **2011**, *331*, 1426–1429.

(4) U.S. Department of Energy Executive Summaries for the Hydrogen Storage Materials Centers of Excellence. 2012; [http://www1.eere.energy.gov/hydrogenandfuelcells/pdfs/executive\\_summaries\\_h2\\_storage\\_coes.pdf](http://www1.eere.energy.gov/hydrogenandfuelcells/pdfs/executive_summaries_h2_storage_coes.pdf), Accessed: 2025-03-26.

(5) Miranda, C. R.; Ceder, G. Ab initio investigation of ammonia-borane complexes for hydrogen storage. *The Journal of chemical physics* **2007**, *126*.

(6) Sa'adeh, H.; Mohamed, A. E.; Richter, R.; Coreno, M.; Wang, F.; Prince, K. C. Photoemission and X-ray Absorption Investigation of Ammonia-Borane in the Gas Phase. *ACS omega* **2023**, *8*, 45970–45975.

(7) Rizzi, V.; Polino, D.; Sicilia, E.; Russo, N.; Parrinello, M. The onset of dehydrogenation in solid ammonia borane: An ab initio metadynamics study. *Angewandte Chemie International Edition* **2019**, *58*, 3976–3980.

(8) Kumar, A.; Eyyathiyil, J.; Choudhury, J. Reduction of carbon dioxide with ammonia-borane under ambient conditions: maneuvering a catalytic way. *Inorganic Chemistry* **2021**, *60*, 11684–11692.

(9) Castilla-Martinez, C. A.; Coşkuner Filiz, B.; Petit, E.; Kantürk Figen, A.; Demirci, U. B. Ammonia borane-based reactive mixture for trapping and converting carbon dioxide. *Frontiers of Materials Science* **2022**, *16*, 220610.

(10) Eland, J. H. D. The Origin of Primary H. *Rapid Communications in Mass Spectrometry* **1996**, *10*, 1560–1562.

(11) Furukawa, Y.; Hoshina, K.; Yamanouchi, K.; Nakano, H. Ejection of triatomic hydrogen molecular ion from methanol in intense laser fields. *Chemical physics letters* **2005**, *414*, 117–121.

(12) Okino, T.; Furukawa, Y.; Liu, P.; Ichikawa, T.; Itakura, R.; Hoshina, K.; Yamanouchi, K.; Nakano, H. Ejection dynamics of hydrogen molecular ions from methanol in intense laser fields. *Journal of Physics B: Atomic, Molecular and Optical Physics* **2006**, *39*, S515.

(13) Dantus, M. Tracking Molecular Fragmentation in Electron–Ionization Mass Spectrometry with Ultrafast Time Resolution. *Accounts of Chemical Research* **2024**, *57*, 845–854.

(14) Dantus, M. Ultrafast studies of elusive chemical reactions in the gas phase. *Science* **2024**, *385*, eadk1833.

(15) Ekanayake, N.; Nairat, M.; Kaderiya, B.; Feizollah, P.; Jochim, B.; Severt, T.; Berry, B.; Pandiri, K. R.; Carnes, K. D.; Pathak, S. et al. Mechanisms and time-resolved dynamics for trihydrogen cation ( $H_3^+$ ) formation from organic molecules in strong laser fields. *Scientific reports* **2017**, *7*, 4703.

(16) Ekanayake, N.; Severt, T.; Nairat, M.; Weingartz, N. P.; Farris, B. M.; Kaderiya, B.; Feizollah, P.; Jochim, B.; Ziaeef, F.; Borne, K. et al. H<sub>2</sub> roaming chemistry and the formation of H<sub>3</sub><sup>+</sup> from organic molecules in strong laser fields. *Nature communications* **2018**, *9*, 5186.

(17) Ekanayake, N.; Nairat, M.; Weingartz, N. P.; Michie, M. J.; Levine, B. G.; Dantus, M. Substituent effects on H<sub>3</sub><sup>+</sup> formation via H<sub>2</sub> roaming mechanisms from organic molecules under strong-field photodissociation. *The Journal of Chemical Physics* **2018**, *149*.

(18) Michie, M. J.; Ekanayake, N.; Weingartz, N. P.; Stamm, J.; Dantus, M. Quantum coherent control of H<sub>3</sub><sup>+</sup> formation in strong fields. *The Journal of Chemical Physics* **2019**, *150*.

(19) Kwon, S.; Sandhu, S.; Shaik, M.; Stamm, J.; Sandhu, J.; Das, R.; Hetherington, C. V.; Levine, B. G.; Dantus, M. What is the Mechanism of H<sub>3</sub><sup>+</sup> Formation from Cyclopropane? *The Journal of Physical Chemistry A* **2023**, *127*, 8633–8638.

(20) Stamm, J.; Priyadarsini, S. S.; Sandhu, S.; Chakraborty, A.; Shen, J.; Kwon, S.; Sandhu, J.; Wicka, C.; Mehmood, A.; Levine, B. G. et al. Factors governing H<sub>3</sub><sup>+</sup> formation from methyl halogens and pseudohalogens. *Nature Communications* **2025**, *16*, 410.

(21) Gope, K.; Livshits, E.; Bittner, D. M.; Baer, R.; Strasser, D. An “inverse” harpoon mechanism. *Science Advances* **2022**, *8*, eabq8084.

(22) Gope, K.; Bittner, D. M.; Strasser, D. Sequential mechanism in H<sub>3</sub><sup>+</sup> formation dynamics on the ethanol dication. *Physical Chemistry Chemical Physics* **2023**, *25*, 6979–6986.

(23) Herbst, E.; Klempner, W. The formation and depletion of molecules in dense interstellar clouds. *The Astrophysical Journal* **1973**, *185*, 505–534.

(24) Oka, T. Interstellar H<sub>3</sub><sup>+</sup>. *Chemical Reviews* **2013**, *113*, 8738–8761.

(25) Luque, P. D. I. T.; Balaji, S.; Silk, J. Anomalous Ionization in the Central Molecular Zone by Sub-GeV Dark Matter. *Physical Review Letters* **2025**, *134*, 101001.

(26) Burrows, M.; Ryan, S.; Lamb Jr, W.; McIntyre Jr, L. Studies of H<sub>+</sub>, H<sub>+</sub> 2, and H<sub>+</sub> 3 dissociative ionization fragments from methane, ethane, methanol, ethanol, and some deuterated methanols using electron-impact excitation and a time-of-flight method incorporating mass analysis. *The Journal of Chemical Physics* **1979**, *71*, 4931–4940.

(27) Hoshina, K.; Kawamura, H.; Tsuge, M.; Tamiya, M.; Ishiguro, M. Metastable decomposition and hydrogen migration of ethane dication produced in an intense femtosecond near-infrared laser field. *The Journal of chemical physics* **2011**, *134*.

(28) Kraus, P. M.; Schwarzer, M. C.; Schirmel, N.; Urbasch, G.; Frenking, G.; Weitzel, K.-M. Unusual mechanism for H<sub>3</sub><sup>+</sup> formation from ethane as obtained by femtosecond laser pulse ionization and quantum chemical calculations. *The Journal of chemical physics* **2011**, *134*.

(29) Schirmel, N.; Reusch, N.; Horsch, P.; Weitzel, K.-M. Formation of fragment ions (H<sub>+</sub>, H<sub>3</sub><sup>+</sup>, CH<sub>3</sub><sup>+</sup>) from ethane in intense femtosecond laser fields—from understanding to control. *Faraday Discussions* **2013**, *163*, 461–474.

(30) Li, S.; Sierra-Costa, D.; Michie, M. J.; Ben-Itzhak, I.; Dantus, M. Control of electron recollision and molecular nonsequential double ionization. *Communications Physics* **2020**, *3*, 35.

(31) Jochim, B.; DeJesus, L.; Dantus, M. Ultrafast disruptive probing: Simultaneously keeping track of tens of reaction pathways. *Review of Scientific Instruments* **2022**, *93*, 033003.

(32) Guo, C.; Li, M.; Nibarger, J. P.; Gibson, G. N. Single and double ionization of diatomic molecules in strong laser fields. *Physical Review A* **1998**, *58*, R4271.

(33) Raghavachari, K.; Trucks, G. W.; Pople, J. A.; Head-Gordon, M. A fifth-order perturbation comparison of electron correlation theories. *Chemical Physics Letters* **1989**, *157*, 479–483.

(34) Bartlett, R. J.; Watts, J.; Kucharski, S.; Noga, J. Non-iterative fifth-order triple and quadruple excitation energy corrections in correlated methods. *Chemical physics letters* **1990**, *165*, 513–522.

(35) Piecuch, P.; Kucharski, S. A.; Kowalski, K.; Musiał, M. Efficient computer implementation of the renormalized coupled-cluster methods: the r-ccsd [t], r-ccsd (t), cr-ccsd [t], and cr-ccsd (t) approaches. *Computer Physics Communications* **2002**, *149*, 71–96.

(36) Piecuch, P.; Włoch, M. Renormalized coupled-cluster methods exploiting left eigenstates of the similarity-transformed Hamiltonian. *The Journal of chemical physics* **2005**, *123*.

(37) Dunning Jr, T. H. Gaussian basis sets for use in correlated molecular calculations. I. The atoms boron through neon and hydrogen. *The Journal of chemical physics* **1989**, *90*, 1007–1023.

(38) Kendall, R. A.; Dunning Jr, T. H.; Harrison, R. J. Electron affinities of the first-row atoms revisited. Systematic basis sets and wave functions. *The Journal of chemical physics* **1992**, *96*, 6796–6806.

(39) Barca, G. M. J.; Bertoni, C.; Carrington, L.; Datta, D.; De Silva, N.; Deustua, J. E.; Fedorov, D. G.; Gour, J. R.; Gunina, A. O.; Guidez, E. et al. Recent developments in the general atomic and molecular electronic structure system. *The Journal of Chemical Physics* **2020**, *152*, 154102.

(40) Purvis III, G. D.; Bartlett, R. J. A full coupled-cluster singles and doubles model: The inclusion of disconnected triples. *The Journal of chemical physics* **1982**, *76*, 1910–1918.

(41) Cullen, J. M.; Zerner, M. C. The linked singles and doubles model: An approximate theory of electron correlation based on the coupled-cluster ansatz. *The Journal of Chemical Physics* **1982**, *77*, 4088–4109.

(42) Woon, D. E.; Dunning Jr, T. H. Gaussian basis sets for use in correlated molecular calculations. III. The atoms aluminum through argon. *The Journal of chemical physics* **1993**, *98*, 1358–1371.

(43) Čížek, J. On the correlation problem in atomic and molecular systems. Calculation of wavefunction components in Ursell-type expansion using quantum-field theoretical methods. *The Journal of Chemical Physics* **1966**, *45*, 4256–4266.

(44) Čížek, J. On the use of the cluster expansion and the technique of diagrams in calculations of correlation effects in atoms and molecules. *Advances in chemical physics* **1969**, *35*–89.

(45) Paldus, J.; Čížek, J.; Shavitt, I. Correlation Problems in Atomic and Molecular Systems. IV. Extended Coupled-Pair Many-Electron Theory and Its Application to the B H 3 Molecule. *Physical Review A* **1972**, *5*, 50.

(46) Shen, J.; Piecuch, P. Doubly electron-attached and doubly ionized equation-of-motion coupled-cluster methods with 4-particle–2-hole and 4-hole–2-particle excitations and their active-space extensions. *The Journal of chemical physics* **2013**, *138*.

(47) Shen, J.; Piecuch, P. Doubly electron-attached and doubly ionised equation-of-motion coupled-cluster methods with full and active-space treatments of 4-particle–2-hole and 4-hole–2-particle excitations: The role of orbital choices. *Molecular Physics* **2014**, *112*, 868–885.

(48) Frisch, M. J.; Trucks, G. W.; Schlegel, H. B.; Scuseria, G. E.;

Robb, M. A.; Cheeseman, J. R.; Scalmani, G.; Barone, V.; Mennucci, B.; Petersson, G. A. et al. Gaussian 09, Revision B.01. 2009.

(49) Chai, J.-D.; Head-Gordon, M. Long-range corrected hybrid density functionals with damped atom–atom dispersion corrections. *Phys. Chem. Chem. Phys.* **2008**, *10*, 6615–6.

(50) Millam, J. M.; Bakken, V.; Chen, W.; Hase, W. L.; Schlegel, H. B. Ab initio classical trajectories on the Born–Oppenheimer surface: Hessian-based integrators using fifth-order polynomial and rational function fits. *The Journal of Chemical Physics* **1999**, *111*, 3800–3805.

(51) Posthumus, J. The dynamics of small molecules in intense laser fields. *Reports on Progress in Physics* **2004**, *67*, 623.

(52) Wang, P.; Sayler, A. M.; Carnes, K. D.; Esry, B. D.; Ben-Itzhak, I. Disentangling the volume effect through intensity-difference spectra: Application to laser-induced dissociation of H 2+. *Optics letters* **2005**, *30*, 664–666.

(53) Wiese, J.; Olivieri, J.-F.; Trabattoni, A.; Trippel, S.; Küpper, J. Strong-field photoelectron momentum imaging of OCS at finely resolved incident intensities. *New Journal of Physics* **2019**, *21*, 083011.

(54) Schleier, D.; Gerlach, M.; Pratim Mukhopadhyay, D.; Karaev, E.; Schaffner, D.; Hemberger, P.; Fischer, I. Ammonia Borane, NH3BH3: A Threshold Photoelectron–Photoion Coincidence Study of a Potential Hydrogen-Storage Material. *Chemistry—A European Journal* **2022**, *28*, e202201378.

(55) Corkum, P. B. Plasma perspective on strong field multiphoton ionization. *Physical review letters* **1993**, *71*, 1994.

(56) Lozovoy, V. V.; Zhu, X.; Gunaratne, T. C.; Harris, D. A.; Shane, J. C.; Dantus, M. Control of molecular fragmentation using shaped femtosecond pulses. *The Journal of Physical Chemistry A* **2008**, *112*, 3789–3812.

(57) De Feyter, S.; Diau, E. W.-G.; Zeewail, A. H. Femtosecond Dynamics of Norrish Type-II Reactions: Nonconcerted Hydrogen-Transfer and Diradical Intermediacy. *Angewandte Chemie* **2000**, *112*, 266–269.

(58) Stamm, J.; Kwon, S.; Sandhu, S.; Shaik, M.; Das, R.; Sandhu, J.; Curenton, B.; Wicka, C.; Levine, B. G.; Sun, L. et al. The surprising dynamics of the mclafferty rearrangement. *The Journal of Physical Chemistry Letters* **2023**, *14*, 10088–10093.

(59) Minvielle, M. K.; Aftel, M.; Hill, T.; Lopez Pena, H. A.; Tibbetts, K. M. How Isomer and Conformer Structures Impact Dissociation Dynamics of Alkane Radical Cations. *The Journal of Physical Chemistry A* **2025**, *129*, 8550–8562.

(60) Frasinski, L.; Codling, K.; Hatherly, P. Covariance mapping: A correlation method applied to multiphoton multiple ionization. *Science* **1989**, *246*, 1029–1031.

(61) Li, Y.; Cavet, G.; Zare, R. N.; Driver, T. Fragment Correlation Mass Spectrometry Enables Direct Characterization of Disulfide Bond Cleavage Pathways of Therapeutic Peptides. *Analytical Chemistry* **2024**, *96*, 15081–15084.

(62) Li, Y.; Cavet, G.; Zare, R. N.; Driver, T. Fragment correlation mass spectrometry: Determining the structures of biopolymers in a complex mixture without isolating individual components. *Proceedings of the national academy of sciences* **2024**, *121*, e2409676121.

(63) Strasser, D.; Livshits, E.; Baer, R. Single-photon double-ionisation coulomb explosion in organic molecules. *International Reviews in Physical Chemistry* **2023**, *42*, 29–51.

(64) Xie, X.; Lötstedt, E.; Roither, S.; Schöffler, M.; Kartashov, D.; Midorikawa, K.; Baltuška, A.; Yamamoto, K.; Kitzler, M. Duration of an intense laser pulse can determine the breakage of multiple chemical bonds. *Scientific reports* **2015**, *5*, 12877.

(65) Ibrahim, H.; Wales, B.; Beaulieu, S.; Schmidt, B. E.; Thiré, N.; Fowe, E. P.; Bisson, É.; Hebeisen, C. T.; Wanie, V.; Giguére, M. et al. Tabletop imaging of structural evolutions in chemical reactions demonstrated for the acetylene cation. *Nature communications* **2014**, *5*, 4422.

(66) Ivanov, M.; Seideman, T.; Corkum, P.; Ilkov, F.; Dietrich, P. Explosive ionization of molecules in intense laser fields. *Physical Review A* **1996**, *54*, 1541.

(67) Newton, A. S.; Sciamanna, A.; Thomas, G. The occurrence of the H3+ ion in the mass spectra of organic compounds. *International Journal of Mass Spectrometry and Ion Physics* **1970**, *5*, 465–482.

(68) Wavefunction Inc. Spartan'24, Version 1.2.0. <https://www.wavefun.com>, 2024; Irvine, CA, USA.

(69) Sloane, C. S.; Hase, W. L. On the dynamics of state selected unimolecular reactions: Chloroacetylene dissociation and predissociation. *The Journal of Chemical Physics* **1977**, *66*, 1523–1533.

(70) Echeverri, A.; Cárdenas, C.; Calatayud, M.; Hadad, C. Z.; Gomez, T. Theoretical analysis of the adsorption of Ammonia-Borane and their dehydrogenation products on the (001) surface of TiC and ZrC. *Surface Science* **2018**,